

# The mass-sheet degeneracy and time-delay cosmography: Analysis of the strong lens RXJ1131-1231

Simon Birrer,<sup>\*</sup> Adam Amara,<sup>†</sup> and Alexandre Refregier<sup>‡</sup>  
*Institute for Astronomy, Department of Physics, ETH Zurich,  
 Wolfgang-Pauli-Strasse 27, 8093, Zurich, Switzerland*

(Dated: May 17, 2022)

We present extended modeling of the strong lens system RXJ1131-1231 with archival data in two HST bands in combination with existing line-of-sight contribution and velocity dispersion estimates. We focus on the accuracy and reliability of the source reconstruction scale and lens model assumptions and its implication on time-delay cosmography. We map out the mass-sheet degeneracy and especially the degeneracy pointed out by Schneider and Sluse [1] using the source reconstruction scale. In a second step, we fold in velocity dispersion and external convergence measurements. We then infer angular diameter distance relations for the time-delays without cosmological priors. For a flat  $\Lambda$ CDM cosmology, these constraints lead to constraints of the Hubble constant  $H_0$  as a function of the matter density  $\Omega_m$  in the form of  $H_0 = H_0^* / [1 + 0.5(\Omega_m - \Omega_m^*)] \pm 5\%$  with  $H_0^* = 71.7^{+3.6}_{-3.6}$  km s<sup>-1</sup>Mpc<sup>-1</sup> being the value for  $H_0$  at  $\Omega_m^* = 0.3$ . This is a significant improvement in the uncertainty of the lens modeling and is consistent with recent CMB measurements. We describe the full cosmological information of the lens system RXJ1131-1231 data in an analytic form such that this information can be combined with other cosmological probes.

## I. INTRODUCTION

Strong lensing systems and the time delays between different images of the same background source can provide information about angular diameter distance relations (see Refsdal [2] and review of Blandford and Narayan [3] for the early work). Cosmographic analyses rely on measurements of time delay [see e.g., 4, and the COSMOGRAIL collaboration] and estimates of the line-of-sight structure and lensing potential. This cosmography technique has been applied to determine the Hubble parameter  $H_0$  using different strong lens systems [see e.g. 5–16] and also by applying statistics to multiple systems [see e.g. 17–19]. In the past, some of the measurements have produced a wide range of results for  $H_0$  [e.g. see section 8.2 of 15]. One concern has been to evaluate the impact of potential systematic errors. In particular, mass-sheet degeneracy (MSD) [20] and related degeneracies that cause biases due to model assumptions [e.g. 5, 21, 22] need special consideration. For instance, this has been illustrated by Schneider and Sluse [1] where they show that assuming a power-law lens model can cause significant biasing of results.

In this paper, we introduce a new treatment of the MSD and source reconstruction for cosmographic analyses. This approach integrates information coming from imaging, velocity dispersion, external convergence and time delay measurements. For the choice of data and the parameterization of the lens we follow the work of Suyu *et al.* [16], and we infer the values of the parameters using our recent framework presented in Birrer *et al.*

[23]. In our framework we reconstruct the source using shapelet basis sets. This allows us to explicitly set an overall scale for the reconstruction. We will show that this enables us to better disentangle the effects coming from source structure and MSD. This then makes it simpler to robustly combine the information coming from the different data sets.

The paper is organized as follow: In Section II we briefly review the principles of time delay cosmography. Section III presents the data used in this work. Section IV describes the details of the lens modeling, including kinematics, likelihood analysis and the source reconstruction technique of Birrer *et al.* [23]. In Section V we show that the use of this reconstruction technique turns out to be well designed for mapping out the MSD. Section VI describes the combined likelihood analysis and posterior sampling. Section VII discuss the cosmological constraints in terms of angular diameter relations and cosmological parameters. In Section VIII, we compare our results to others. We summarize our conclusions in Section IX.

## II. THEORY

Gravitational lensing is caused by deflection of light by matter. In this section, we review the principles of gravitational lensing and time delay cosmography and introduce our conventions.

<sup>\*</sup> simon.birrer@phys.ethz.ch

<sup>†</sup> adam.amara@phys.ethz.ch

<sup>‡</sup> alexandre.refregier@phys.ethz.ch

### A. Lensing formalism

The lensing potential  $\psi(\vec{\theta})$  at an angular position  $\vec{\theta} = (\theta_1, \theta_2)$  is given by

$$\psi(\vec{\theta}) = \frac{1}{\pi} \int d^2\vec{\theta}' \kappa(\vec{\theta}') \ln |\vec{\theta} - \vec{\theta}'| \quad (1)$$

where  $\kappa$  is the convergence and is given by

$$\kappa(\vec{\theta}) = \frac{\Sigma(D_d \vec{\theta})}{\Sigma_{\text{crit}}} \quad (2)$$

where

$$\Sigma_{\text{crit}} = \frac{c^2 D_s}{4\pi G D_d D_{\text{ds}}} \quad (3)$$

is the critical density and  $\Sigma(D_d \vec{\theta})$  is the physical projected surface mass density.  $D_d$ ,  $D_s$  and  $D_{\text{ds}}$  are the angular diameter distances from the observer to the lens, to the source and from the lens to the source<sup>1</sup>, respectively. The deflection angle is  $\vec{\alpha}(\vec{\theta}) = \vec{\nabla}\psi(\vec{\theta})$  and the lens equation, which describes the mapping from the source plane  $\vec{\beta} = (\beta_1, \beta_2)$  to the image plane  $\vec{\theta}$  is given by

$$\vec{\beta} = \vec{\theta} - \vec{\alpha}(\vec{\theta}). \quad (4)$$

The convergence  $\kappa(\vec{\theta})$  can also be written as

$$\kappa(\vec{\theta}) = \frac{1}{2} \nabla^2 \psi(\vec{\theta}). \quad (5)$$

### B. Time delays

The Fermat potential is defined as

$$\phi(\vec{\theta}, \vec{\beta}) \equiv \left[ \frac{(\vec{\theta} - \vec{\beta})^2}{2} - \psi(\vec{\theta}) \right]. \quad (6)$$

The excess time delay of an image at  $\vec{\theta}$  with corresponding source position  $\vec{\beta}$  is

$$t(\vec{\theta}, \vec{\beta}) = \frac{D_{\Delta t}}{c} \phi(\vec{\theta}, \vec{\beta}) \quad (7)$$

where

$$D_{\Delta t} \equiv (1 + z_d) \frac{D_d D_s}{D_{\text{ds}}} \quad (8)$$

is referred as the time delay distance. The relative time delay difference  $\Delta t_{ij}$  between two images positioned at  $\vec{\theta}_i$  and  $\vec{\theta}_j$ , the actual observable, is then given by

$$\Delta t_{ij} = t_i(\vec{\theta}_i, \vec{\beta}) - t_j(\vec{\theta}_j, \vec{\beta}). \quad (9)$$

<sup>1</sup>  $D_{\text{ds}}$  is *not* the subtraction  $D_d - D_s$ . In a flat universe:  $D_{\text{ds}} = \frac{1}{1+z_s}(M_d - M_s)$ , where  $M$  is the transverse co-moving distance.

Line-of-sight (LOS) structures external to the lens also affect the observed time delay distance through additional focusing or de-focusing of the light rays. We parameterize the LOS structure with a single constant mass sheet parameter  $\kappa_{\text{ext}}$ , the external convergence. The actual time delay distance  $D_{\Delta t}$  relates to the one inferred by ignoring the external LOS structure is related by

$$D_{\Delta t} = \frac{D_{\Delta t}^{\text{model}}}{1 - \kappa_{\text{ext}}} \quad (10)$$

## III. RXJ1131-1231 SYSTEM

The quadrupole lens system RXJ1131-1231 (Figure 1) was discovered by [24] and the redshift of the lens  $z_l = 0.295$  and of the background quasar source  $z_s = 0.658$  was determined spectroscopically [24]. The lens was modeled extensively by [16, 23, 25, 26] with single band images. We use the archival HST ACS WFC1 images in filter F814W and F555W (GO 9744; PI: Kochanek). The filter F814W was also used for lens modeling in [16] and [23]. We make use of the `MultiDrizzle` product from the HST archive. We use a  $160^2$  pixel image centered at the lens position.

For the analysis in this work, we use the time delay measurements and uncertainties from [27], namely  $\Delta t_{AB} = 0.7 \pm 1.4$  days,  $\Delta t_{CB} = -0.4 \pm 2.0$  days, and  $\Delta t_{DB} = 91.4 \pm 1.5$  days, where  $[A, B, C, D]$  represent the quasar images in Figure 1. This data was used in [16], where they also measure the LOS velocity dispersion of  $\sigma_v = 323 \pm 20$  km s<sup>-1</sup>, that we use in our analysis.

For the external convergence  $\kappa_{\text{ext}}$ , we take the estimate of [16] based on relative galaxy counts in the field and their modeled external shear component compared with ray tracing of the Millennium Simulation (see their Figure 6). As their probability density function for  $\kappa_{\text{ext}}$  is not given in a parameterized form, we use an approximation of their PDF in the form of a skewed normal distribution with mean  $\mu_\kappa = 0.1$ , standard deviation  $\sigma_\kappa = 0.042$  and skewness  $\gamma_\kappa = 0.8$ . This function is illustrated in Figure 2 and described in Appendix C.

## IV. LENS MODELING

In this section, we present the parameterization of the lens model, the lens light description, the source reconstruction technique, PSF modeling, the modeling of the lens kinematics and the likelihood analysis.

### A. Lens model parameterization

For the lens model, we use:

1. An elliptical power-law mass distribution parame-

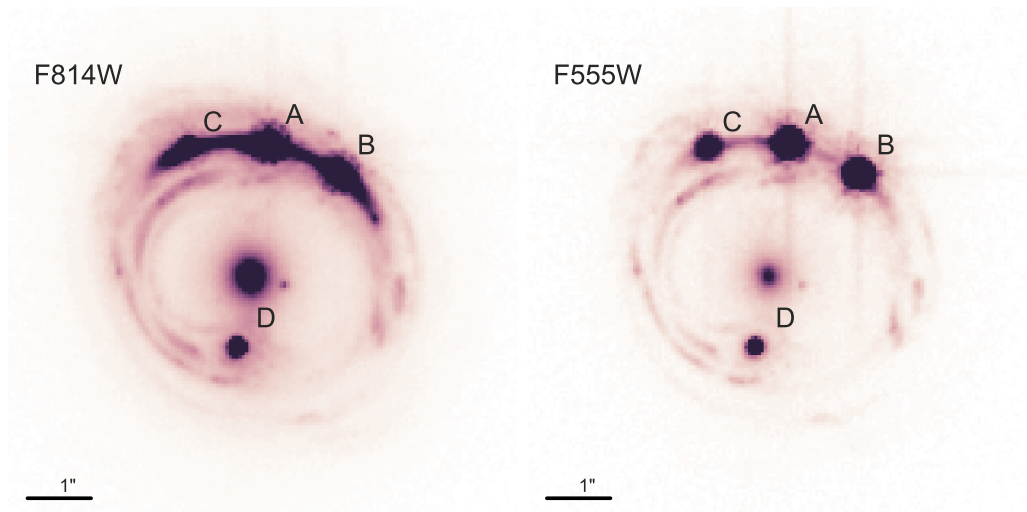


FIG. 1. HST ACS WFC1 images in filters F814W (left) and F555W (right). The F814W filter has more high signal-to-noise pixels than the F555W filter. In the F555W filter, the substructure in the Einstein ring and the diffraction spikes of the quasar images are more prominent. The letters A,B,C,D indicate the quasar images for the time delay differences.

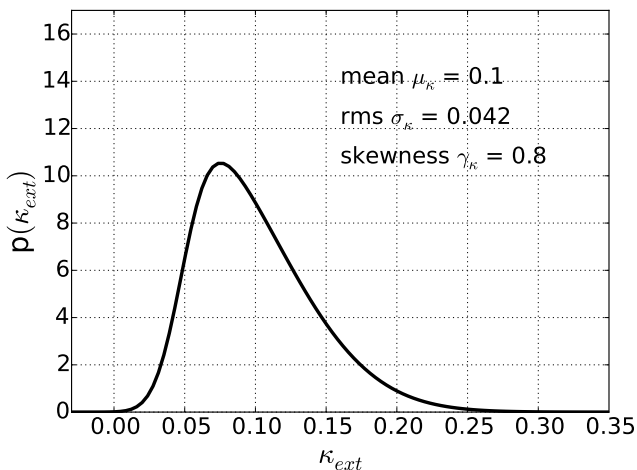


FIG. 2. Probability density function of the external convergence in the form of a skewed normal distribution. The parameters chosen are designed to match well the probability density function quoted in [16] (their Figure 6).

terized as

$$\kappa_{\text{lens}}(\theta_1, \theta_2) = \frac{3 - \gamma'}{2} \left( \frac{\theta_E}{\sqrt{q\theta_1^2 + \theta_2^2/q}} \right)^{\gamma' - 1} \quad (11)$$

with  $\theta_E$  is the Einstein radius,  $q$  is the ellipticity and  $\gamma'$  is the radial power-law slope.

2. A second spherical isothermal profile (Equation 11 with fixed  $\gamma' = 2$  and  $q = 1$ ) centered at the position of the visible companion of the lens galaxy about 0.6 arc seconds away from the center.

3. A constant external shear yielding a potential parameterized in polar coordinates  $(\theta, \varphi)$  given by

$$\psi_{\text{ext}}(\theta, \varphi) = \frac{1}{2} \gamma_{\text{ext}} \theta^2 \cos 2(\varphi - \phi_{\text{ext}}) \quad (12)$$

with  $\gamma_{\text{ext}}$  is the shear strength and  $\phi_{\text{ext}}$  is the shear angle.

### B. Lens light parameterization

The light distribution of the lens is modeled in a parameterized form. We use the same profiles as [16], namely two elliptical Sérsic profiles [28] with common centroid for the central elliptical galaxy and an additional spherical Sérsic profile for the companion galaxy. The intensity profile is parameterized as

$$I(\theta_1, \theta_2) = A \exp \left[ -k \left( \left( \frac{\sqrt{\theta_1^2 + \theta_2^2/q_L^2}}{r_{\text{eff}}} \right)^{1/n_{\text{Sersic}}} - 1 \right) \right] \quad (13)$$

where  $A$  is the amplitude,  $k$  is a constant such that  $r_{\text{eff}}$  is the effective half-light radius,  $q_L$  is the axis ratio and  $n_{\text{Sersic}}$  is the Sérsic index. We use the value of half-light radius  $r_{\text{eff}}$  as the effective radius in the kinematics modeling of Section IV E.

### C. Source surface brightness reconstruction

We use the source reconstruction method presented in [23] based on shapelet basis functions introduced by [29]. To apply this method, three choices have to be made. (1) The shapelet center position, which we fixed to the

quasar position. (2) The width of the shapelet basis function  $\beta$  (see Section V for its impact). (3) The maximal order  $n_{\max}$  of the shapelet polynomials. We set  $n_{\max} = 30$  for modeling and parameter inference. With this, most of the features in the extended source can be modeled. Given these three choices, one can reconstruct the scales between  $\beta/\sqrt{n_{\max} + 1}$  and  $\beta\sqrt{n_{\max} + 1}$  around the center of the shapelet in the source plane.

#### D. PSF modeling

We use four bright stars in the same ACS image to model the PSF. After normalizing for flux, we apply a sub-pixel shift to recenter the stars and then stack. When comparing the individual star images and the stack, we see significant variations that we need to consider in our analysis. To do this by measuring the scatter for each pixel and assume that the scatter in high signal-to-noise pixels is due to a model error that we quantify as a fraction of the flux. This leads to an additional error term, beyond the Poisson and background contribution, that is important close to the center of the bright point sources (see Section IV F). For the quasar point sources, we use a cutout of the PSF of  $111^2$  pixels to cover most of the diffraction spikes. For the extended surface brightness we apply a convolution kernel of  $21^2$  pixels.

#### E. Stellar kinematics

We follow the analysis of [15] for the modeling of the stellar velocity dispersion. The velocity dispersion modeling relies on cosmological information. This fact is important when kinematic modeling is used to infer cosmographic information. We separate in the modeling the angular and the cosmological information. The separability allows us to consistently infer cosmographic information without giving cosmological priors in the kinematic modeling.

The mass profile is assumed to be a spherical symmetric power-law in the form of

$$\rho_{\text{local}}(r) = \rho_0 \left( \frac{r_0}{r} \right)^{\gamma'} \quad (14)$$

where  $\rho_0$  is the density at radius  $r_0$  and  $\gamma'$  is a power-law slope of the mass profile (the same  $\gamma'$  as for the lens model in Equation 11). The normalization of the mass profile can be expressed in terms of the lensing quantities as

$$\rho_0 r_0^{\gamma'} = (\kappa_{\text{ext}} - 1) \Sigma_{\text{crit}} \theta_E^{\gamma'-1} D_d^{\gamma'-1} \frac{\Gamma\left(\frac{\gamma'}{2}\right)}{\pi^{1/2} \Gamma\left(\frac{\gamma'-3}{2}\right)}. \quad (15)$$

where  $\kappa_{\text{ext}}$  is the external convergence,  $\Sigma_{\text{crit}}$  is the critical projected density,  $\theta_E$  is the Einstein radius,  $D_d$  is the angular diameter distance from the observer to the lens

and  $\Gamma$  is the Gamma function. Assuming a Hernquist profile [30] and an anisotropy radius  $r_{\text{ani}}$  for the stellar orbits in the lens galaxy, the stellar velocity dispersion from Jeans modeling is given by

$$\sigma_v^2 = (\kappa_{\text{ext}} - 1) \frac{4\pi G a^{-\gamma'} \rho_0 r_0^{\gamma'}}{3 - \gamma'} \frac{r(r+a)^3}{r^2 + r_{\text{ani}}^2} J(a, r, r_{\text{ani}}, \gamma') \quad (16)$$

with

$$J(a, r, r_{\text{ani}}, \gamma') = \left( \frac{r_{\text{ani}}^2}{a^2} \frac{{}_2F_1\left[2 + \gamma', \gamma'; 3 + \gamma'; \frac{1}{1+r/a}\right]}{(2 + \gamma')(r/a + 1)^{2+\gamma'}} + \frac{{}_2F_1\left[3, \gamma'; 1 + \gamma'; -a/r\right]}{\gamma'(r/a)^{\gamma'}} \right), \quad (17)$$

where  $a$  is related to the effective radius of the lens  $r_{\text{eff}}$  by  $a = 0.551 r_{\text{eff}}$  and  ${}_2F_1$  is a hypergeometric function. Equation (16) can be expressed as a function of an angular scale  $r$  with a cosmological dependent term  $F(\boldsymbol{\pi})$  (where  $\boldsymbol{\pi}$  are the cosmological parameters, e.g.  $\Lambda$ CDM), a cosmological independent term  $H(\gamma', \theta_E, r_{\text{ani}}, r_{\text{eff}}, r)$  and a pre-factor with  $\kappa_{\text{ext}}$  as

$$\sigma_v^2(r) = (\kappa_{\text{ext}} - 1) \cdot F(\boldsymbol{\pi}) \cdot H(\gamma', \theta_E, r_{\text{ani}}, r_{\text{eff}}, r) \quad (18)$$

with

$$H = \frac{4\pi^{1/2} G}{3 - \gamma'} \frac{\Gamma\left(\frac{\gamma'}{2}\right)}{\Gamma\left(\frac{\gamma'-3}{2}\right)} \frac{\theta_E^{\gamma'-1}}{a^{\gamma'}} \frac{r(r+a)^3}{r^2 + r_{\text{ani}}^2} J(a, r, r_{\text{ani}}, \gamma') \quad (19)$$

and

$$F = \Sigma_{\text{crit}}(\boldsymbol{\pi}, z_d) D_d(\boldsymbol{\pi}, z_d) \quad (20)$$

With this calculation, we see that any estimate of the (central) velocity dispersion is dependent on the ratio of angular diameter distance from us to the source and from the deflector to the source (combine Equation 3, 18 and 20)

$$\sigma_v^2 = \frac{c^2}{4\pi} (\kappa_{\text{ext}} - 1) \frac{D_s}{D_{\text{ds}}} H(\gamma', \theta_E, r_{\text{ani}}, r_{\text{eff}}, r). \quad (21)$$

#### F. Likelihood analysis

We estimate the pixel uncertainty in the image with a Gaussian background contribution  $\sigma_{\text{bgd}}$  estimated from a empty region in the image and a Poisson contribution from the model signal  $d_{\text{p},i}$  scaled by the exposure map  $t_i$ . In addition, the modeling uncertainty of the PSF of the bright point sources with amplitude  $A_j$ , PSF kernel  $k_{ij}$  and model uncertainty coming from the star-by-star scatter  $\delta_{\text{PSF}}$  is given as

$$\sigma_{\text{PSF},i} = \sum_{j=1}^{N_{\text{AGN}}} A_j k_{ij} \delta_{\text{PSF},ij}, \quad (22)$$

at a pixel  $i$ , where  $N_{\text{AGN}}$  is the number of quasar images. All together, the uncertainty for each pixel  $i$  sums up in quadrature as

$$\sigma_{\text{pixel},i}^2 = \sigma_{\text{bgd}}^2 + t_i^{-1} d_{\text{P},i} + \sigma_{\text{PSF},i}^2. \quad (23)$$

For the linear source surface brightness reconstruction  $d_{\text{P},i}$  is replaced by the image intensity  $d_{\text{ACS},i}$ .

The likelihood of an image  $\mathbf{d}_{\text{ACS}}$  given a model  $\mathbf{d}_{\text{P}}$  is

$$P(\mathbf{d}_{\text{ACS}}|\mathbf{d}_{\text{P}}) = \frac{1}{Z_{\text{d}}} \exp \sum_{i=1}^{N_{\text{d}}} \left[ -\frac{(d_{\text{ACS},i} - d_{\text{P},i})^2}{2\sigma_{\text{pixel},i}^2} \right] \quad (24)$$

with  $N_{\text{d}}$  being the number of pixel in the modeled image and  $Z_{\text{d}}$  is the normalization

$$Z_{\text{d}} = (2\pi)^{N_{\text{d}}/2} \prod_i \sigma_{\text{pixel},i}. \quad (25)$$

At this stage, it is useful to separate the model into nonlinear parameters  $\boldsymbol{\eta}$  and linear parameters  $\mathbf{s}$ . The likelihood of the non-linear parameters is given by

$$P(\mathbf{d}_{\text{ACS}}|\boldsymbol{\eta}) = \int d\mathbf{s} P(\mathbf{d}_{\text{ACS}}|\boldsymbol{\eta}, \mathbf{s}) P(\mathbf{s}). \quad (26)$$

The integral is computed in [23] (their Equation 13) assuming flat priors in  $\mathbf{s}$ , which we adopt.

The likelihood for the time delays  $\Delta \mathbf{t}$  is the product of the likelihoods of all relative delays of the quasar pairs ( $ab$ )

$$P(\Delta \mathbf{t} | D_{\Delta \mathbf{t}}^{\text{model}}, \boldsymbol{\eta}) = \prod_{(ab)} \left( \frac{1}{\sqrt{2\pi}\sigma_{ab}} \exp \left[ -\frac{(\Delta t_{ab} - \Delta t_{ab}^{\text{P}})^2}{2\sigma_{ab}^2} \right] \right). \quad (27)$$

The likelihood of the LOS central velocity dispersion is given by

$$P(\sigma_v | \boldsymbol{\eta}) = \frac{1}{\sqrt{2\pi}\sigma_{\sigma}} \exp \left[ -\frac{(\sigma_v - \sigma^{\text{P}})^2}{2\sigma_{\sigma}^2} \right]. \quad (28)$$

## V. THE MASS SHEET DEGENERACY

There exists many different degeneracies in strong lens modeling [e.g., 21, 31]. In this section we focus on the MSD [20] and in particular its impact on time delay cosmography as it was pointed out by [1]. As shown by [20], a remapping of a reference mass distribution  $\kappa$  by

$$\kappa_{\lambda}(\vec{\theta}) = \lambda \kappa(\vec{\theta}) + (1 - \lambda) \quad (29)$$

combined with an isotropic scaling of the source plane coordinates

$$\vec{\beta} \rightarrow \lambda \vec{\beta} \quad (30)$$

will result in the same dimensionless observables (image positions, image shapes and magnification ratios) regardless of the value of  $\lambda$ . This type of mapping is called mass-sheet-transform (MST), and shows that imaging data, no matter how good, can not break the MSD.

The additional mass term in MST (Equation 29) can be internal to the lens galaxy (affecting the lens kinematics) or due to line-of-sight structure (not affecting the lens kinematics) [see e.g., 21, 22]. The external part of the MST can be approximated by an external convergence  $\kappa_{\text{ext}}$ , which rescales the time delays accordingly. The external contribution also rescales the source plane. Lens modeling often only explicitly models the internal structure of the lens. The inferred source scale has to be rescaled by the external mass sheet to match the physical scale.

As pointed out by [1], there can also be an internal component to the MST. Namely when the lens model can not reproduce the underlining internal mass distribution. The assumption of a power-law lens model formally sets the internal part of the MST. The parameters will fit preferentially those models, whose shape, modulo an artificial MST, are the most similar to the underlying mass distribution. The only effect visible in the modeling of the imaging data is on the source scale. The inferred source scale will be different from the one inferred from the true lens model. Any assumed mass distribution which can not be rescaled according to Equation (29) can thus potentially lead to biased inferences, in particular on the slope of the mass profile. This also can result in significant biases in the inferred lensing potential and lens kinematics. In particular, it was stated by [1] that the assumption of a power-law lens model can potentially lead to a significant bias in the inference of the time delay distance.

### A. Source scaling and the MSD

Another important parameter other than the assumed lens mass profile is the physical source scale. Neither the lens model nor the source size are direct observables, but they share the MST in each others inference. Given a lens model, certain source sizes are preferred. The opposite is also true: Given a source size, certain lens models are preferred. This is a direct consequence of the MST (Equation 29 and 30). Therefore, it is important to control the prior on the assumed source scale in the modeling. A particular source surface brightness reconstruction method, depending on the choice of regularization, basis set, pixel grid size or parameters of the source reconstruction, will potentially favor a certain size of the reconstructed source and therefore may indirectly lead to priors on the internal mass model through the MST. As one does not know a priori the physical scales in the source galaxy, this may lead to significant biases in the inference of the lens model.

We use shapelets [29] as the source surface brightness

basis functions as implemented in [23]. These basis functions form a complete basis set when the order  $n$  goes to infinity. When restricting the shapelet basis to a finite order  $n_{\text{max}}$ , the reconstruction of an image depends on the chosen scale  $\beta$  of the shapelet basis function. As pointed out by [29], for a given  $n_{\text{max}}$ , there is a scale  $\hat{\beta}$  that best fits the data. From Equation 30, we see that changes in  $\beta$  can be remapped into changes in the lensing potential through the linear parameter  $\lambda$ . Therefore, since our source reconstruction technique has an explicit scale, we have a tool to walk along the MST.

### B. Varying source scale in the ACS WFC1 images

We have identified two model assumptions (shapelet scale and power-law mass profile), that have an impact on the inference of the lens model within the MST. To investigate the dependence on the combination of shapelet scale and mass profile in our analysis of RXJ1131-1231, we model the ACS WFC1 F814W and F555W images with different choices of the shapelet scale  $\beta$ . For the F814W image, we use the range 0.14" - 0.19" and for the F555W image the range 0.13" - 0.18". The shapelet order was held constant at  $n_{\text{max}} = 30$ . To find the best fit model, we used a particle swarm optimization as used in [23] to maximize the likelihood (Equation 26).

Figure 3 shows the source reconstruction of the best fit models of filter F814W for six different scales  $\beta$ . We see that the source reconstructions are very similar but scaled by the relative factors of the chosen shapelet scale. More explicitly, we overlay in Figure 4 the intensity contours of the different source reconstructions rescaled by  $\beta$ . We also show the reconstructions for the F555W image, which shows the same behavior. On the right of Figure 4 we over-plot a joint source reconstruction of the two bands in a fake color image. In Appendix A, we present the corresponding normalized residuals for this analysis of the F814W reconstruction.

We note that the lens model parameterization used (see Section IV A) does not allow for the full freedom needed for a perfect transform according to the MST (Equation 29). Any deviation of the best fit lens model can reduce the likelihood (Equation 26). However, we find that for this specific example the imposed scales in the source surface brightness reconstruction dominates the imaging likelihood.

### C. Adding lens kinematics

To overcome the spurious effect in the source surface brightness reconstruction, one can assign a flat prior to  $\beta$ . We would then be left with the assumption on the mass profile as discussed in depth in [1]. The posterior distribution in the lens model parameters would lie at the position where, modulo an arbitrary MST, the power-law mass model is similar to the underlying true mass

distribution.

Additional constraints on the lens model can come from kinematic data at a different scale than the Einstein ring. Transformations according to the MST lead to different predictions on the lens kinematics. The prediction depends on the anisotropy radius  $r_{\text{ani}}$  which can not be known from the existing data and the external convergence  $\kappa_{\text{ext}}$  which has to be inferred separately.

We note that the difference in the likelihood value for different scales  $\beta$  from the imaging data exceeds the 10- $\sigma$  level between each modeled scale  $\beta$ . As long as the relative likelihood of additional kinematic data (Equation 28) can not compete with the relative likelihood of the different shapelet scales  $\beta$ , the combined likelihood will be dominated by the lens model assumption. Only when re-normalizing the likelihood of the imaging data for different scales  $\beta$ , the kinematic data will have a significant impact in the determination of the lens profile.

## VI. COMBINED LIKELIHOOD ANALYSIS

In this section, we discuss how we combine the different data sets and their likelihoods. We showed in the previous section that biases can emerge from choices in the lens and source modeling. These aspects have to be taken into account when the datasets are combined.

### A. Combining imaging and time delay data

In a first step, we do a joint analysis of the independent measurements of the time delay and imaging data. We do not yet combine the kinematic data at the likelihood level. The combined likelihood is

$$P(\mathbf{d}_{\text{ACS}}, \Delta\mathbf{t}|\boldsymbol{\eta}, D_{\Delta t}^{\text{model}}) = P(\mathbf{d}_{\text{ACS}}|\boldsymbol{\eta})P(\Delta\mathbf{t}|D_{\Delta t}^{\text{model}}, \boldsymbol{\eta}) \quad (31)$$

with the independent likelihoods of Equation (26) and (27). We sample all the lens model parameters and the time delay distance  $D_{\Delta t}^{\text{model}}$ . We keep the lens light parameters fixed at the final position of the particle swarm process. We do not expect a significant impact on the results on the remaining parameters.

From Bayes theorem, the likelihood of the parameters given the data is (modulo a normalization):

$$P(\boldsymbol{\eta}, D_{\Delta t}^{\text{model}}|\mathbf{d}_{\text{ACS}}, \Delta\mathbf{t}) \propto P(\mathbf{d}_{\text{ACS}}, \Delta\mathbf{t}|\boldsymbol{\eta}, D_{\Delta t}^{\text{model}})P(\boldsymbol{\eta})P(D_{\Delta t}^{\text{model}}). \quad (32)$$

We apply flat priors on the parameters  $\gamma' \in [1, 2.8]$ ,  $\theta_E \in [0.1'', 10'']$ ,  $q \in [0.5, 1]$ ,  $\theta_{E, \text{clump}} \in [0'', 1'']$ ,  $\gamma_{\text{ext}} \in [0, 0.3]$  and  $D_{\Delta t}^{\text{model}} \in [0, 10'000]$  Mpc.

At this stage, we want to emphasize that there are 3 data points in the time delay measurement compared to several thousands of high signal-to-noise pixels in the imaging comparison. In principle, the provided time delay measurement can not only determine  $D_{\Delta t}^{\text{model}}$ , which

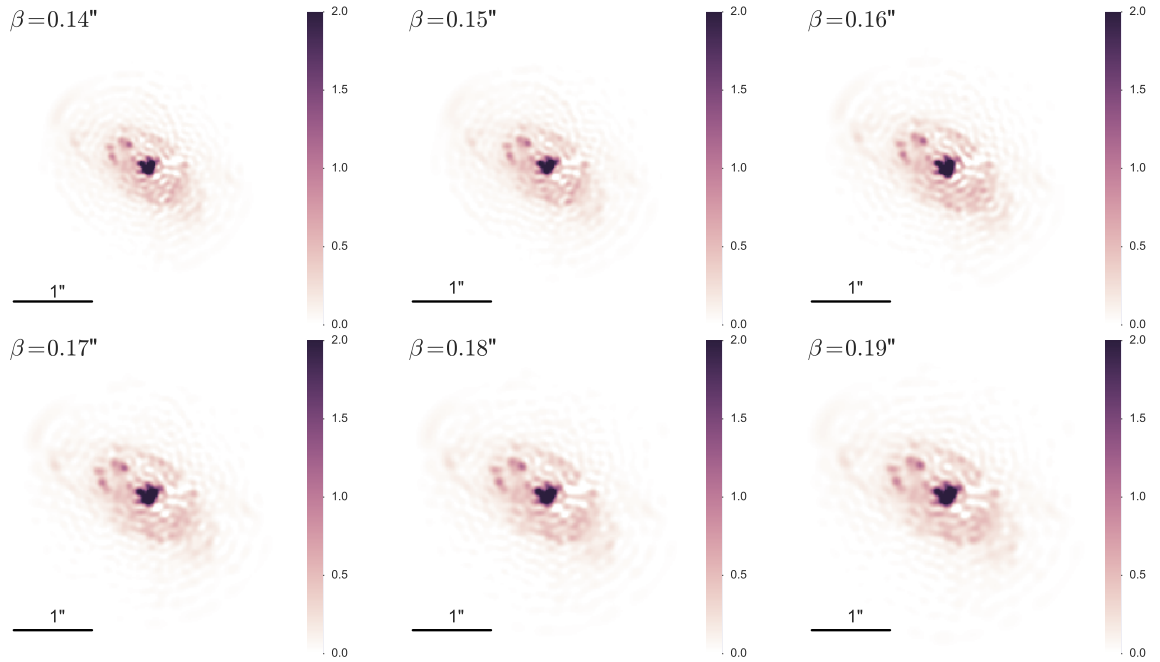


FIG. 3. Reconstructed source surface brightness profiles as a function of shapelet scale  $\beta$  for filter F814W. The source reconstructions of the best fit lens model configurations are shown with a given  $\beta$ . We see that the features become larger with larger choices of  $\beta$ .

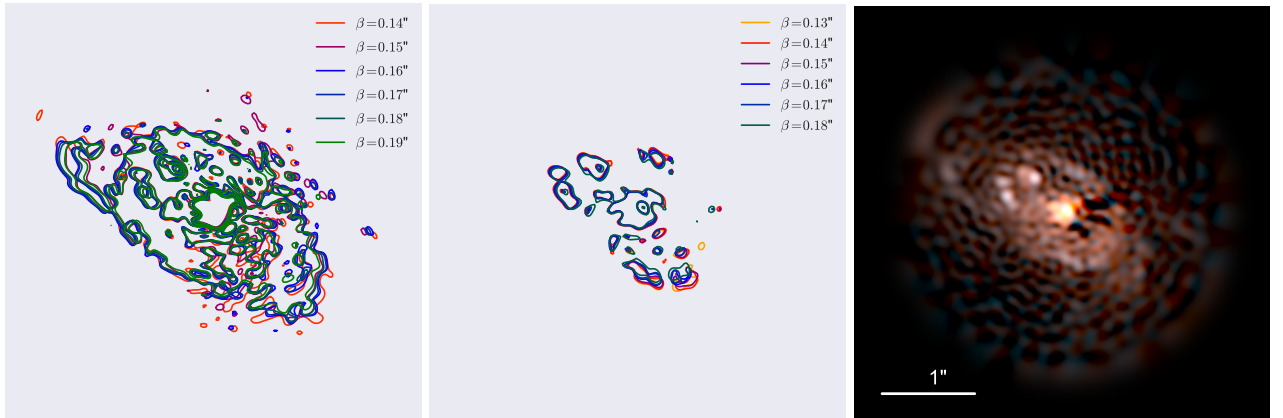


FIG. 4. Left: Intensity contours of the reconstructed source surface profiles rescaled to fiducial value  $\beta = 0.2''$  for the different shapelet scales  $\beta$  in filter F814W of Figure 3. The contour lines overlay well. The lens model does adopt to the choice of  $\beta$  such that the source reconstruction catches the best scales. Middle: Same as left for the filter F555W. The same behavior can be seen as for F814W. Right: Color composite model of the filters F814W and F555W for a chosen joint lens model.

is independent of the imaging data but also can partially constrain the lens model. In practice, any even minor bias introduced in the image modeling can out-weigh the constraining power of the two additional time delay measurements.

In the following, we present the results of the analysis of filter F814W. The results of the equivalent analysis of filter F555W can be found in Appendix B. To sample the posterior distribution of the parameter space we use *CosmoHammer* [32]. We fix the shapelet scale  $\beta$  at  $[0.14'', 0.15'', 0.16'', 0.17'', 0.18'', 0.19'']$  and do a separate in-

ference of the parameters for each choice of  $\beta$ . Figure 5 shows the posterior distribution of some of the parameters for the different choices of  $\beta$ . The inferred parameter constraints for different  $\beta$  values do not overlap. We see that  $\gamma_{\text{ext}}$  is very narrowly determined for a given shapelet scale  $\beta$  but varies from 0.07 up to 0.11 depending on the position in the degeneracy plane. We want to stress that the external convergence  $\kappa_{\text{ext}}$  estimate of [16] is based on an external shear prior of  $\gamma_{\text{ext}} = 0.089 \pm 0.006$ .

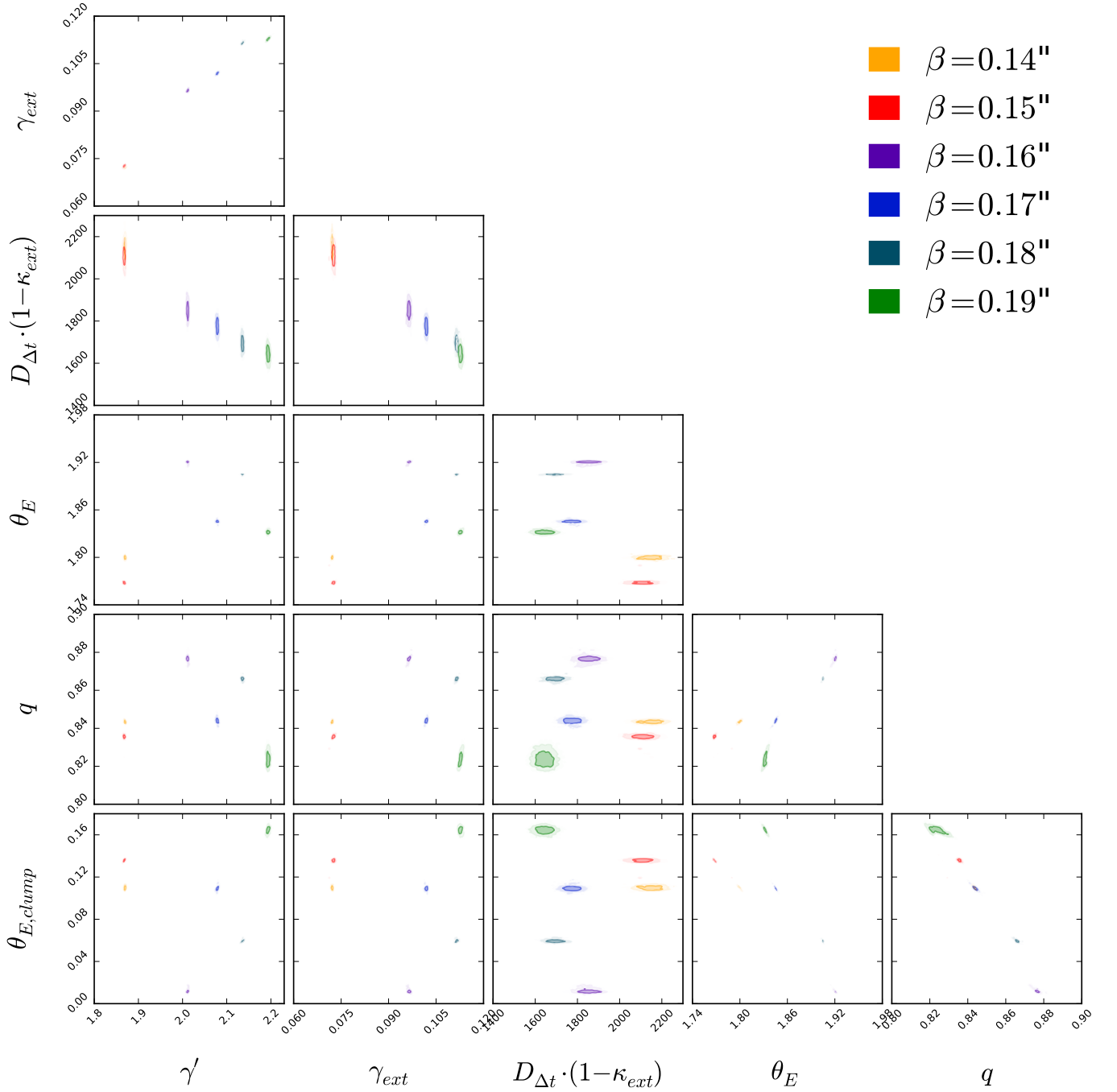


FIG. 5. Posterior distribution of lens model parameters and time delay distance of the combined analysis of imaging data of F814W and time delay measurements. Different colors correspond to different choices of the shapelet scale  $\beta$ . The posterior samples for different  $\beta$  values mutually disagree in almost all parameters presented.

### B. Constraints from kinematic data

To investigate the potential constraining power of the velocity dispersion data, we are interested in how distinguishable different positions within the MST are in terms of their predicted central velocity dispersions. To do so, we fix the cosmology and the external convergence  $\kappa_{\text{ext}}$  to a fiducial values. This allows us to evaluate the pre-

dicted LOS central velocity dispersion  $\sigma_v$  (Equation 21) for all the posterior samples of Figure 5. We assume a random realization of  $r_{\text{ani}}$  with a flat prior in the range  $[0.5, 5]$  for all the posterior positions.

In Figure 6 we illustrate the predicted  $\sigma_v$  samples vs the predicted time delay distance  $D_{\Delta t}$ . We see that most samples can clearly be distinguished with the current velocity dispersion measurement and its uncertainty of



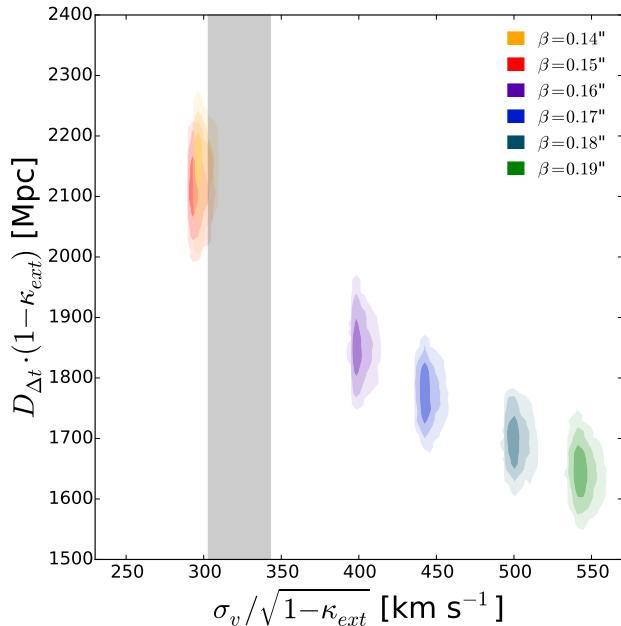


FIG. 6. Estimated LOS central velocity dispersions  $\sigma_v$  vs. time delay distances  $D_{\Delta t}$  of the sample of lens models from Figure 5 (in the same colors). The external convergence  $\kappa_{ext}$  was explicitly left out of the analysis and the cosmology has been fixed to the Planck mean values in this particular plot. The gray band reflects the  $1\text{-}\sigma$  uncertainty range of the LOS velocity dispersion estimates from the data. This shows that velocity dispersion estimates add important information on the lens model constraints.

$\pm 20 \text{ km s}^{-1}$ . Furthermore, the error of  $\pm 20 \text{ km s}^{-1}$  in the central velocity dispersion measure can be translated in a relative error in the time delay distance  $D_{\Delta t}$  of about 2.0%. An accurate and precise model of the kinematic data is important for the cosmological inference.

The relative distance in the predicted velocity dispersion  $\sigma_v$  between the different samples are all within  $10\sigma$  (from kinematic uncertainties). In Section V C we showed that the individual image likelihoods of the different  $\beta$  samples differ by more than  $10\sigma$ .

Before folding in the velocity dispersion measurement in our cosmographic analysis, we re-normalize the image likelihood such that it is independent of the source scale  $\beta$  and the position in the MST. This re-normalization is done by taking the same number of MCMC posterior samples from the different source scales  $\beta$  when doing further inferences with the lens model parameters.

## VII. COSMOLOGICAL INFERENCE

In this section, we study the cosmological constraints from strong lensing using data from images, time delays, central velocity dispersion of the lensing galaxy and independent external convergence estimates. Strong lensing

systems are sensitive to angular diameter distance, which can in turn be used to measure cosmological parameters. We first show the data can be used to constrain the angular diameter relation. Based on the constraints on the angular diameter distances, we then introduce the likelihood that allows us to infer the parameters within the flat  $\Lambda$ CDM cosmological model.

### A. Angular diameter distance posteriors

We can combine the posterior samples of Figure 5 with the independent velocity dispersion measurement to calculate the angular diameter distance relations  $D_d$  and  $D_s/D_{ds}$  (Equation 21 and 8) as

$$\frac{D_s}{D_{ds}} = \frac{4\pi G}{c^2} \frac{\sigma_{r=0}^2}{(\kappa_{ext} - 1)} \frac{1}{H(\gamma', \theta_E, r_{ani}, r_{eff}, r=0)} \quad (33)$$

and

$$D_d = \frac{D_{\Delta t}^{model}}{(1+z_d)(1-\kappa_{ext})} \frac{D_{ds}}{D_s}. \quad (34)$$

To take into account the errors in  $\sigma_v$ ,  $\kappa_{ext}$  and  $r_{ani}$ , we importance sample the posteriors from the independent measurements ( $\sigma_v$  and  $\kappa_{ext}$ ) and for  $r_{ani}$  we uniformly sample in the range  $[0.5, 5]$  times  $r_{eff}$  [see e.g. 15, 16, 33, for similar use].

The  $D_d$  vs  $D_s/D_{ds}$  plane as shown in Figure 7 inherits the cosmological information of this analysis coming from the combined data and consistently translates the uniform prior in the source scale into the cosmological inference. This plane covers a large range but the constrained region is narrow. We over-plot the posterior samples of WMAP DR9 [34] and Planck15 [35] converted to the angular diameter distances of the lens system. We find consistent results to those from the CMB experiments in a flat  $\Lambda$ CDM cosmology for the low redshift angular diameter distance relations and the strong lens system RXJ1131-1231.

### B. An analytic likelihood for cosmology

So far, we have discretized the degeneracy plane by uniformly sample  $\beta$  in steps of 0.01". Effectively this means that while all the other parameters are sampled through standard MCMC methods, the  $\beta$  direction is sampled on a grid. This separation is needed to allow us to do the re-normalization of the likelihood as described in Section VIB. Sampling the  $\beta$ -grid finely is computationally expensive. In the following, we show how we can analytically describe the posterior distribution and fill the gaps in  $\beta$  without additional sampling.

To do so, we first map the  $D_d$  vs  $D_s/D_{ds}$  plane of Figure 7 (left panel) into a  $\ln D_d$  vs  $D_{ds}/(D_d D_s)$  plane (right panel). We see a linear relations between the posterior samples in a monotonic and equally spaced increasing

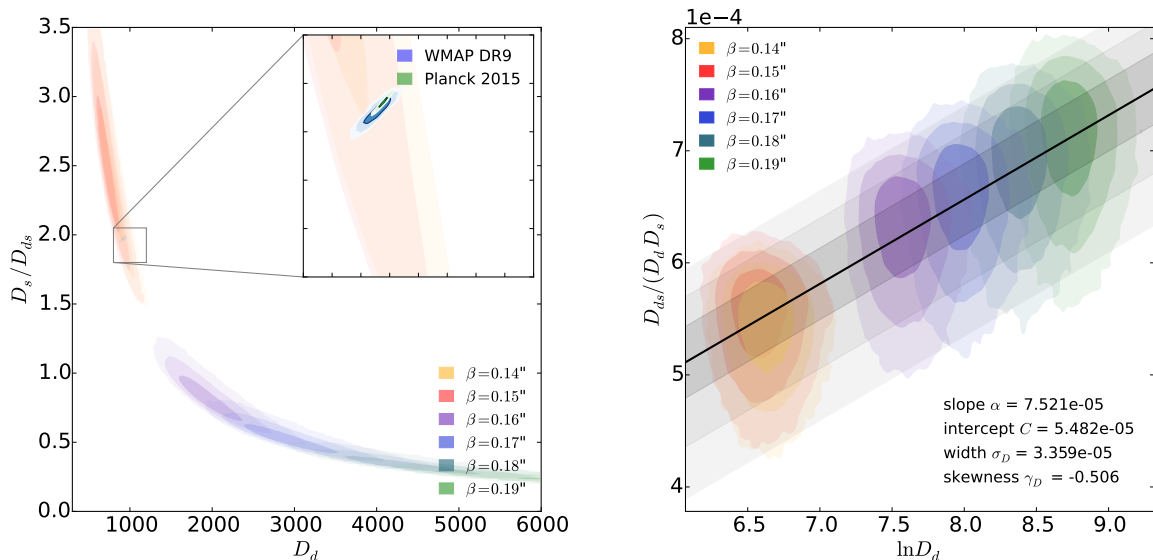


FIG. 7. The constraints of the angular diameter distance relation for discrete positions in the MSD plane for filter F814W (same analysis for filter F555W is shown in Figure 11 in the appendix). Different colors indicate different positions in the MSD. On the left panel:  $D_d$  vs  $D_s/D_{ds}$ . Also over-plotted are the posteriors of the WMAP DR9 and Planck 2015  $\Lambda$ CDM posteriors mapped in the same angular diameter distance relation. On the right panel: Re-mapping of the angular diameter relations into a  $\ln D_d$  vs  $D_{ds}/(D_d D_s)$  plane. The linear fit is indicated by the thick black line and the (1,2,3)- $\sigma$  upper and lower limits of the projected distribution are plotted in different grey scale. The parameters of the fit are indicated in the figure.

fashion as a function of  $\beta$ . We fit with linear regression the function

$$\frac{D_{ds}}{D_d D_s} = \alpha \ln(D_d) + C \quad (35)$$

with  $\alpha$  being the slope and  $C$  being the intercept. The legend of Figure 7 (right panel) shows the best fit values, which we discuss in more detail later. The linear fit is a good description of the combined samples of different source scalings. The same is shown for the filter F555W analysis in Appendix B. The spread of the distribution orthogonal to the linear relation is not well fit by a Gaussian distribution, but we find a skewed normal distribution provides a good description.

The one-dimensional likelihood  $P(\mathbf{d}_{\text{RXJ}}, \boldsymbol{\pi})$  of the strong lens system data  $\mathbf{d}_{\text{RXJ}}$  given a cosmological model  $\boldsymbol{\pi}$  is given by the one-dimensional probability density of the samples relative to the fitted line:

$$P(\mathbf{d}_{\text{RXJ}}, \boldsymbol{\pi}) = \phi_\gamma \left( x = \frac{D_{ds}}{D_d D_s}, \mu = \alpha \ln(D_d) + C, \sigma_D, \gamma_D \right), \quad (36)$$

where  $\sigma_D$  is the standard deviation,  $\gamma_D$  the skewness and  $\phi_\gamma$  is the re-parameterized skewed normal distribution function described in Appendix C. For the analysis of the HST band F814W we fit the values  $C = 5.5 \cdot 10^{-5}$ ,  $\alpha = 7.52 \cdot 10^{-5}$ ,  $\sigma_D = 3.359 \cdot 10^{-5}$  and  $\gamma_D = -0.506$ . For band F555W the fits result in  $C = -1.66 \cdot 10^{-5}$ ,  $\alpha = 8.69 \cdot 10^{-5}$ ,  $\sigma_D = 3.416 \cdot 10^{-5}$  and  $\gamma_D = -0.473$ . The units of these parameters are given in respect with the angular diameter distances in co-moving Mpc.

The simple form of the likelihood enables a fast and consistent combination of different strong lensing systems also in combination with other cosmological probes.

### C. Cosmological parameter constraints

The constraints on the angular diameter distance relations can be turned into constraints on the cosmological parameters of the background evolution. In the following we assume a flat  $\Lambda$ CDM cosmology. The homogeneous expansion can be described in terms of the matter density  $\Omega_m$  and the Hubble constant  $H_0$ . We use the likelihood of Equation (36) with the values of  $\alpha$ ,  $C$ ,  $\sigma_D$  and  $\gamma_D$  from the analysis of F814W and F555W separately. First, we sample the parameters  $\Omega_m$  and  $H_0$  simultaneously with uniform priors of  $\Omega_m \in [0, 1]$  and  $H_0 \in [0, 200]$ . Figure 8 shows the posterior distributions for the filter F814W (left panel) and F555W (middle panel) separately. The degeneracy in  $\Omega_m$  is strong but  $H_0$  can be determined fairly well. A good approximation of the degeneracy shown in the  $H_0$ - $\Omega_m$ -plane can be described by

$$H_0 = H_0^* \left[ 1 + \frac{1}{2}(\Omega_m - \Omega_m^*) \right]^{-1} \pm \sigma_{H_0^*} \left( \frac{H_0}{H_0^*} \right) \quad (37)$$

where  $H_0^*$  is the value for  $H_0$  at fixed  $\Omega_m^*$  and  $\sigma_{H_0^*}$  is the marginalized error at fixed  $\Omega_m^*$ . This form allows us to more directly compare with other results from the literature.

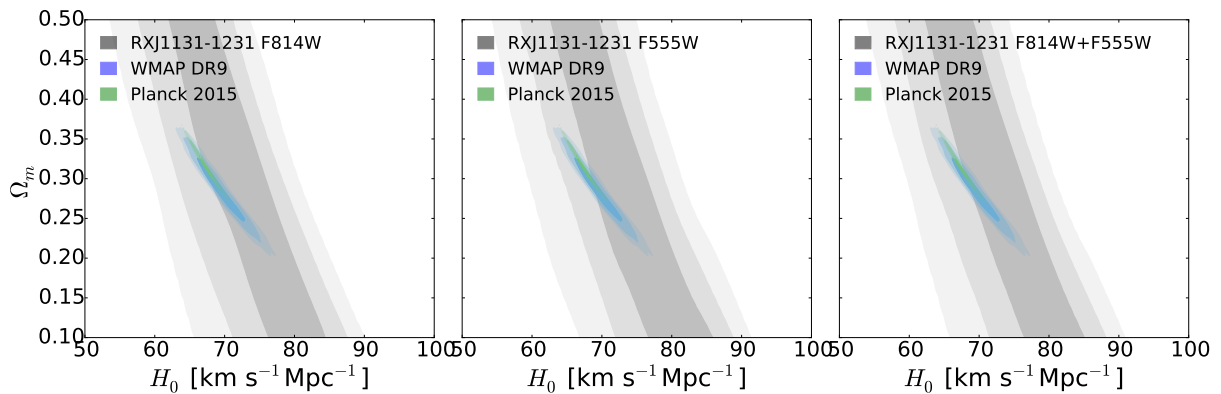


FIG. 8. Posterior sampling of the cosmological parameters for the filters F814W (left), F555W (middle) and combined with equal weight of the likelihoods of the two images (right). The posterior distribution of WMAP DR9 and Planck 2015 are over-plotted.

For a fixed value of  $\Omega_m = 0.3$ , we infer a Hubble constant of  $H_0 = 71.5^{+3.5}_{-3.6} \text{ km s}^{-1} \text{ Mpc}^{-1}$  for the F814W and  $H_0 = 72.1^{+3.5}_{-3.5} \text{ km s}^{-1} \text{ Mpc}^{-1}$  for the F555W analysis.

From the analysis of each filter separately, we get an uncertainty coming from the imaging data only to be below 1% in the resulting inference of  $H_0$ . Given the fact that our estimates for the two filters F814W and F555W is about 1.5% different while using exactly the same analysis for all other parameters involved, we conclude that the imaging data inference is partially driven by unknown systematics in the modeling and the data. To marginalize out potential systematics in the analysis, we combine the two analyses with equal weight in their likelihoods. The two-dimensional posteriors are shown in the right panel of Figure 8. In this way, we get a Hubble constant of  $H_0 = 71.7^{+3.6}_{-3.6} \text{ km s}^{-1} \text{ Mpc}^{-1}$ . The full posteriors for both samples are shown in Figure 9.

### VIII. JOINT UNCERTAINTIES AND COMPARISON WITH OTHER WORK

In Table I the estimated uncertainties from the different data sets are summarized. The Gaussian approximation of all these errors leads to a total uncertainty of 5.5% on  $H_0$ . The estimate of the uncertainty coming from the full sampling results in 5.0%. This is an improvement in precision compared to [16], who state an error of 6% on  $H_0$  with the same data sets. Furthermore, the mean value of [16] was higher with  $H_0 = 78.7^{+4.3}_{-4.5} \text{ km s}^{-1} \text{ Mpc}^{-1}$  for a value of  $\Omega_m = 0.27$ . This is a shift of about  $1.5 \sigma$  in their stated uncertainty. The main difference between the two results arise from the explicit treatment of the MSD and related degeneracies in our work and its link to the source surface brightness reconstruction method. We use explicit uniform priors on the source scale. This allows us to work in a 2D-plane (Figure 7) of angular diameter distance relations and to overcome (at least partially) systematics from the source reconstruction method and

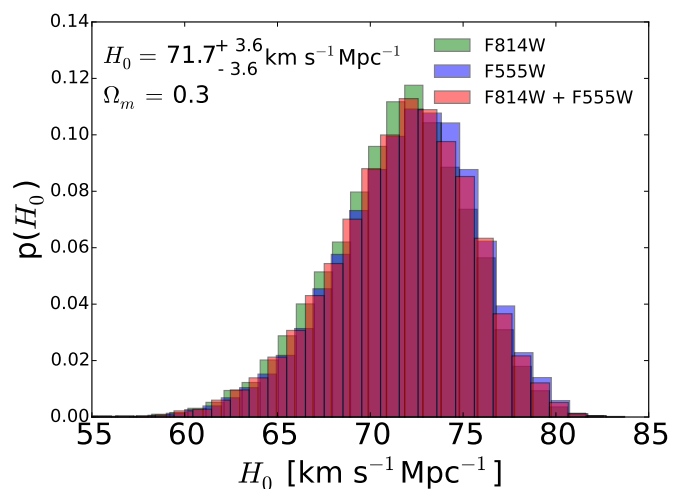


FIG. 9. Posterior distribution for the value of  $H_0$  for a fixed  $\Omega_m = 0.3$  for filter F814W (green), F555W (blue) and the combined samples (red).

the mass profile assumption.

Comparing our results with the CMB experiments, we get consistent results on the  $\Lambda$ CDM parameter. The angular diameter distance at last scattering and the inferred angular diameter distance relation at lower redshift from this analysis are therefore consistent with a  $\Lambda$ CDM cosmology.

We also emphasize that the uncertainty in  $\kappa_{\text{ext}}$  of 4.7% has the largest impact on the uncertainty in the cosmological constraints. Reducing the error to  $\sigma_{\kappa} = [0.03, 0.02, 0.01]$  will directly lead to measurements of  $H_0$  to about [4.2%, 3.5%, 3.2%] precision without any further change in the analysis or other data components presented in this work. 3% is the limit beyond which other uncertainties and systematics become dominant.

TABLE I. Error budget on  $H_0$  for a fixed  $\Omega_m$ .

Description	Uncertainty
Time delays	1.6%
Lens mass model	0.9%
Line-of-sight contribution	4.7%
Lens kinematics	2.0%
Total (Gaussian)	5.5%
Total (full sampling <sup>a</sup> )	5.0%

<sup>a</sup> The uncertainty in the full sampling is given as half of the 68% confidence interval divided by the mean posterior value.

## IX. CONCLUSIONS

In this work we applied the newly developed source reconstruction technique of Birrer *et al.* [23] to the strong lens system RXJ1131-1231 to extract cosmographic information. We showed how different reconstruction scales probe different regimes in the MST even when the lens model is not fully transformable through the MST.

This work is built on the modeling and the data of [16] and the systematics analysis of [1]. We incorporate a re-normalization of the imaging likelihood such that we have uniform priors on the source scale before combining with the kinematic data.

We introduced a cosmographic inference analysis

which enables us to combine imaging, time-delay and kinematic data without relying on any cosmological priors. We came up with a likelihood function only based on the angular diameter distance relations, which can be described in analytic terms.

From the strong lens system RXJ1131-1231 analysis alone, we can draw the posterior samples of  $\Omega_m$  vs.  $H_0$ . When fixing  $\Omega_m = 0.3$ , we get an estimate of the Hubble constant of  $H_0 = 71.7^{+3.6}_{-3.6}$  km s<sup>-1</sup>Mpc<sup>-1</sup>, a precision of about 5%. The dominant component of the uncertainty in the cosmological inference comes from the line-of-sight contribution. Narrowing down this uncertainty can lead to a precision in  $H_0$  of about 4% or below.

This inference analysis was achieved with a single strong lens system in two imaging bands. Combining the information of multiple systems with comparable data can add vital constraints about the late time expansion history of the universe, also in terms of extensions of the standard cosmological model.

## ACKNOWLEDGMENTS

We acknowledge the import, partial use or inspiration of the following python packages: CosmoHammer [36], FASTELL [37], numpy <sup>2</sup>, scipy <sup>3</sup>, astropy <sup>4</sup>, triangle <sup>5</sup>. This work has been supported by the Swiss National Science Foundation (grant 200021\_149442/1 and 200021\_143906/1).

- 
- [1] P. Schneider and D. Sluse, *Astronomy & Astrophysics* **559**, A37 (2013).
  - [2] S. Refsdal, *Monthly Notices of the Royal Astronomical Society* **128**, 307 (1964).
  - [3] R. D. Blandford and R. Narayan, In: *Annual review of astronomy and astrophysics*. Vol. 30 (A93-25826 09-90) **30**, 311 (1992).
  - [4] A. Eigenbrod, F. Courbin, C. Vuissoz, G. Meylan, P. Saha, and S. Dye, *Astronomy and Astrophysics* **436**, 25 (2005).
  - [5] P. Schneider and C. Seitz, *Astronomy and Astrophysics* (ISSN 0004-6361) **294**, 411 (1995).
  - [6] C. S. Kochanek, *Astrophysical Journal* v.466 **466**, 638 (1996).
  - [7] P. L. Schechter, C. D. Bailyn, R. Barr, R. Barvainis, C. M. Becker, G. M. Bernstein, J. P. Blakeslee, S. J. Bus, A. Dressler, E. E. Falco, R. A. Fesen, P. Fischer, K. Gebhardt, D. Harmer, J. N. Hewitt, J. Hjorth, T. Hurt, A. O. Jaunsen, M. Mateo, D. Mehlert, D. O. Richstone, L. S. Sparke, J. R. Thorstensen, J. L. Tonry, G. Wegner, D. W. Willmarth, and G. Worthey, *The Astrophysical Journal*

- 475**, L85 (1997), (c) 1997: The American Astronomical Society.
- [8] L. V. E. Koopmans, T. Treu, C. D. Fassnacht, R. D. Blandford, and G. Surpi, *The Astrophysical Journal* **599**, 70 (2003).
- [9] O. Wucknitz, A. D. Biggs, and I. W. A. Browne, *Monthly Notices of the Royal Astronomical Society* **349**, 14 (2004).
- [10] T. York, N. Jackson, I. W. A. Browne, O. Wucknitz, and J. E. Skelton, *Monthly Notices of the Royal Astronomical Society* **357**, 124 (2005).
- [11] P. Jakobsson, J. Hjorth, I. Burud, G. Letawe, C. Lidman, and F. Courbin, *Astronomy and Astrophysics* **431**, 103 (2005).
- [12] C. Vuissoz, F. Courbin, D. Sluse, G. Meylan, M. Ibrahimov, I. Asfandiyarov, E. Stoops, A. Eigenbrod, L. L. Guillou, H. V. Winckel, and P. Magain, *Astronomy and Astrophysics* **464**, 845 (2007).
- [13] D. Paraficz, J. Hjorth, and Á. Elíasdóttir, *Astronomy and Astrophysics* **499**, 395 (2009).
- [14] R. Fadely, C. R. Keeton, R. Nakajima, and G. M. Bernstein, *The Astrophysical Journal* **711**, 246 (2010).
- [15] S. H. Suyu, P. J. Marshall, M. W. Auger, S. Hilbert, R. D. Blandford, L. V. E. Koopmans, C. D. Fassnacht, and T. Treu, *The Astrophysical Journal* **711**, 201 (2010).
- [16] S. H. Suyu, M. W. Auger, S. Hilbert, P. J. Marshall, M. Tewes, T. Treu, C. D. Fassnacht, L. V. E. Koopmans, D. Sluse, R. D. Blandford, F. Courbin, and G. Meylan,

---

<sup>2</sup> [www.numpy.org](http://www.numpy.org)

<sup>3</sup> [www.scipy.org](http://www.scipy.org)

<sup>4</sup> [www.astropy.org](http://www.astropy.org)

<sup>5</sup> <https://github.com/dfm/triangle.py>

- The Astrophysical Journal **766**, 70 (2013).
- [17] P. Saha, J. Coles, A. V. Macciò, and L. L. R. Williams, The Astrophysical Journal **650**, L17 (2006).
  - [18] M. Oguri, The Astrophysical Journal **660**, 1 (2007).
  - [19] J. Coles, The Astrophysical Journal **679**, 17 (2008).
  - [20] E. E. Falco, M. V. Gorenstein, and I. I. Shapiro, Astrophysical Journal **289**, L1 (1985).
  - [21] P. Saha, The Astronomical Journal **120**, 1654 (2000).
  - [22] O. Wucknitz, Monthly Notices of the Royal Astronomical Society **332**, 951 (2002).
  - [23] S. Birrer, A. Amara, and A. Refregier, arXiv **astro-ph.CO** (2015), 1504.07629v1.
  - [24] D. Sluse, J. Surdej, J.-F. Claeskens, D. Hutsemékers, C. Jean, F. Courbin, T. Nakos, M. Billeres, and S. V. Khmil, Astronomy and Astrophysics **406**, L43 (2003).
  - [25] J.-F. Claeskens, D. Sluse, P. Riaud, and J. Surdej, Astronomy and Astrophysics **451**, 865 (2006).
  - [26] B. J. Brewer and G. F. Lewis, Monthly Notices of the Royal Astronomical Society **390**, 39 (2008).
  - [27] M. Tewes, F. Courbin, G. Meylan, C. S. Kochanek, E. Eulaers, N. Cantale, A. M. Mosquera, I. Asfandiyarov, P. Magain, H. V. Winckel, D. Sluse, R. K. S. Keerthi, C. S. Stalin, T. P. Prabhu, P. Saha, and S. Dye, The Messenger **150**, 49 (2012).
  - [28] J. Sersic, Atlas de galaxias australes (1968).
  - [29] A. Refregier, Monthly Notice of the Royal Astronomical Society **338**, 35 (2003).
  - [30] L. Hernquist, Astrophysical Journal **356**, 359 (1990).
  - [31] P. Saha and L. L. R. Williams, The Astrophysical Journal **653**, 936 (2006).
  - [32] J. Akeret, S. Seehars, A. Amara, A. Refregier, and A. Csillaghy, Astronomy and Computing **2**, 27 (2013).
  - [33] A. Lewis and S. Bridle, Physical Review D **66**, 103511 (2002).
  - [34] G. Hinshaw, D. Larson, E. Komatsu, D. N. Spergel, C. L. Bennett, J. Dunkley, M. R. Nolta, M. Halpern, R. S. Hill, N. Odegard, L. Page, K. M. Smith, J. L. Weiland, B. Gold, N. Jarosik, A. Kogut, M. Limon, S. S. Meyer, G. S. Tucker, E. Wollack, and E. L. Wright, The Astrophysical Journal Supplement **208**, 19 (2013).
  - [35] Planck, arXiv **astro-ph.CO** (2015), 1502.01589v2.
  - [36] J. Akeret, S. Seehars, A. Amara, A. Refregier, and A. Csillaghy, Astrophysics Source Code Library , 1303.003 (2013).
  - [37] R. Barkana, Astrophysical Journal v.502 **502**, 531 (1998).

### Appendix A: Residual maps

In Figure 10 the normalized residuals corresponding to the source models with different source scales  $\beta$  in Section VB are shown. The residual maps differ significantly between the best fit values of the different shapelet scales  $\beta$ . This reflects the fact that extended structure in the Einstein ring can give constraints on the local slope of the mass profile and the given mass model can not adopt

equally well to different source scales as it is can not be rescaled according to the mass-sheet transform. The inferred lens models can be understood as the best fit power-law profiles at different positions within the MST.

### Appendix B: Analysis on WFC1 F555W

In the paper, we did focus on the analysis of the WFC1 F814W filter band. Here we present the same analysis for filter F555W. Figure 12 shows the posterior distribution of the lens model parameters and time delay distance for F555W. Figure 11 shows the constraints on the angular diameter distance relation. The values describing the distribution can be found in the main text.

### Appendix C: Skewed normal distribution

The the skewed normal distribution is defined with a parameter  $\alpha$  as

$$\phi_\gamma(x) = 2\phi(x)\Phi(\alpha x) \quad (C1)$$

with  $\phi(x)$  being the standard normal probability density function and  $\Phi(x)$  its cumulative distribution. Location and scale can be added with

$$x \rightarrow \frac{x - \xi}{\omega}. \quad (C2)$$

The mean  $\mu$  of this distribution is given by

$$\mu = \xi + \omega\delta\sqrt{\frac{2}{\pi}} \quad (C3)$$

where

$$\delta = \frac{\alpha}{\sqrt{1 + \alpha^2}}. \quad (C4)$$

The variance  $\sigma^2$  is

$$\sigma^2 = \omega^2 \left(1 - \frac{2\delta^2}{\pi}\right) \quad (C5)$$

and the skewness  $\gamma$  as

$$\gamma = \frac{4 - \pi}{2} \frac{\left(\delta\sqrt{2/\pi}\right)^3}{(1 - 2\delta^2/\pi)^{3/2}}. \quad (C6)$$

The skewed normal distribution  $\phi_\gamma(x, \xi, \omega, \alpha)$  can be re-parameterized to  $\phi_\gamma(x, \mu, \sigma, \gamma)$  by inverting the equations (C3)-(C6).

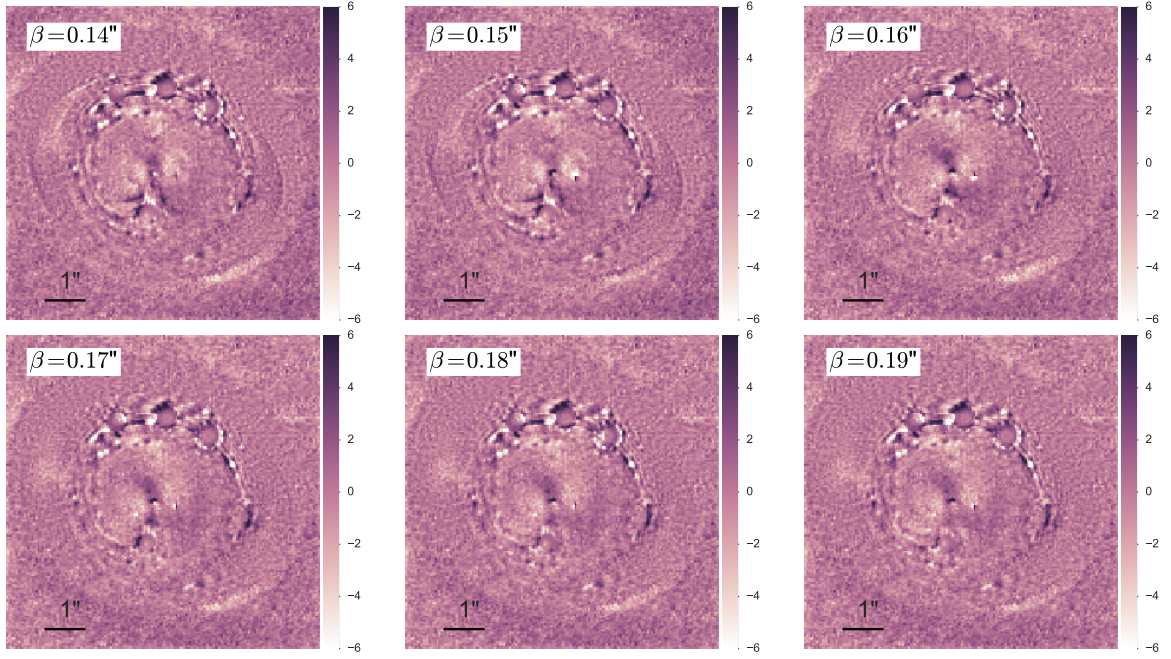


FIG. 10. The normalized residual maps for the best fit reconstruction for the different choices of the shapelet scale  $\beta$  for the F814W image. The residuals differ significantly for the different choices of  $\beta$ . From the imaging data only, a scale  $\beta = 0.19''$  is favored over a scale  $\beta = 0.14''$  by more than  $30\sigma$ . This statement is entirely lens model dependent.

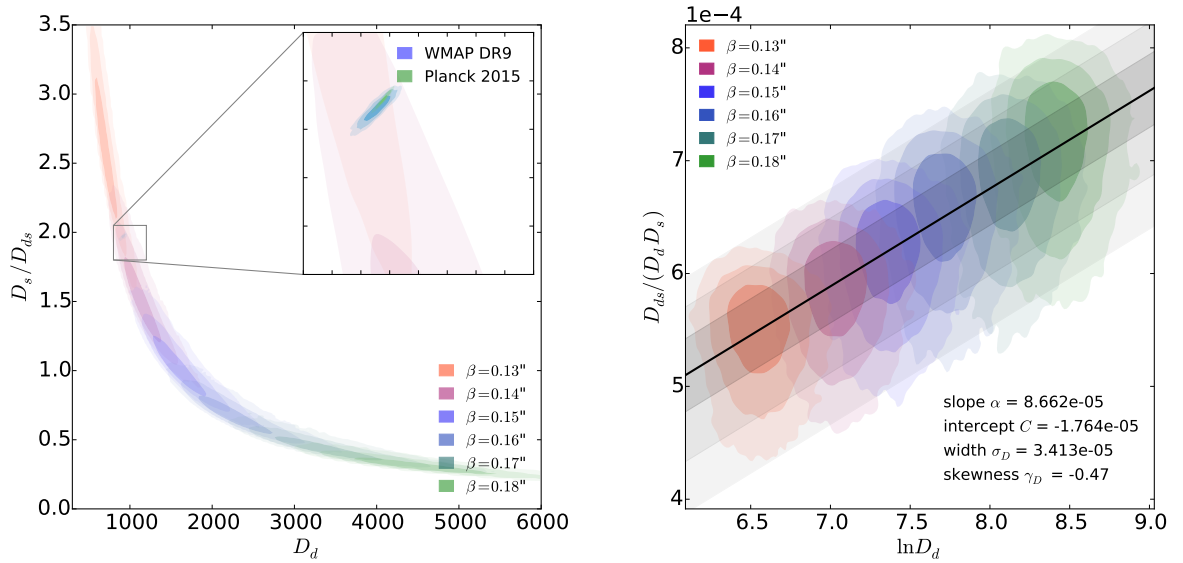


FIG. 11. The constraints of the angular diameter distance relation for discrete positions in the MSD plane for filter F555W (same as Figure 7 for filter F814W). Different colors indicate different source scales. On the left panel:  $D_d$  vs  $D_s/D_{ds}$ . Also over-plotted are the posteriors of the WMAP DR9 and Planck 2015  $\Lambda$ CDM posteriors mapped in the same angular diameter distance relation. On the right panel: Re-mapping of the angular diameter relations into a  $\ln D_d$  vs  $D_{ds}/(D_d D_s)$  plane. The linear fit is indicated by the thick black line and the (1,2,3)- $\sigma$  upper and lower limits of the projected distribution are plotted in gray scale. The parameters of the fit are indicated in the figure.



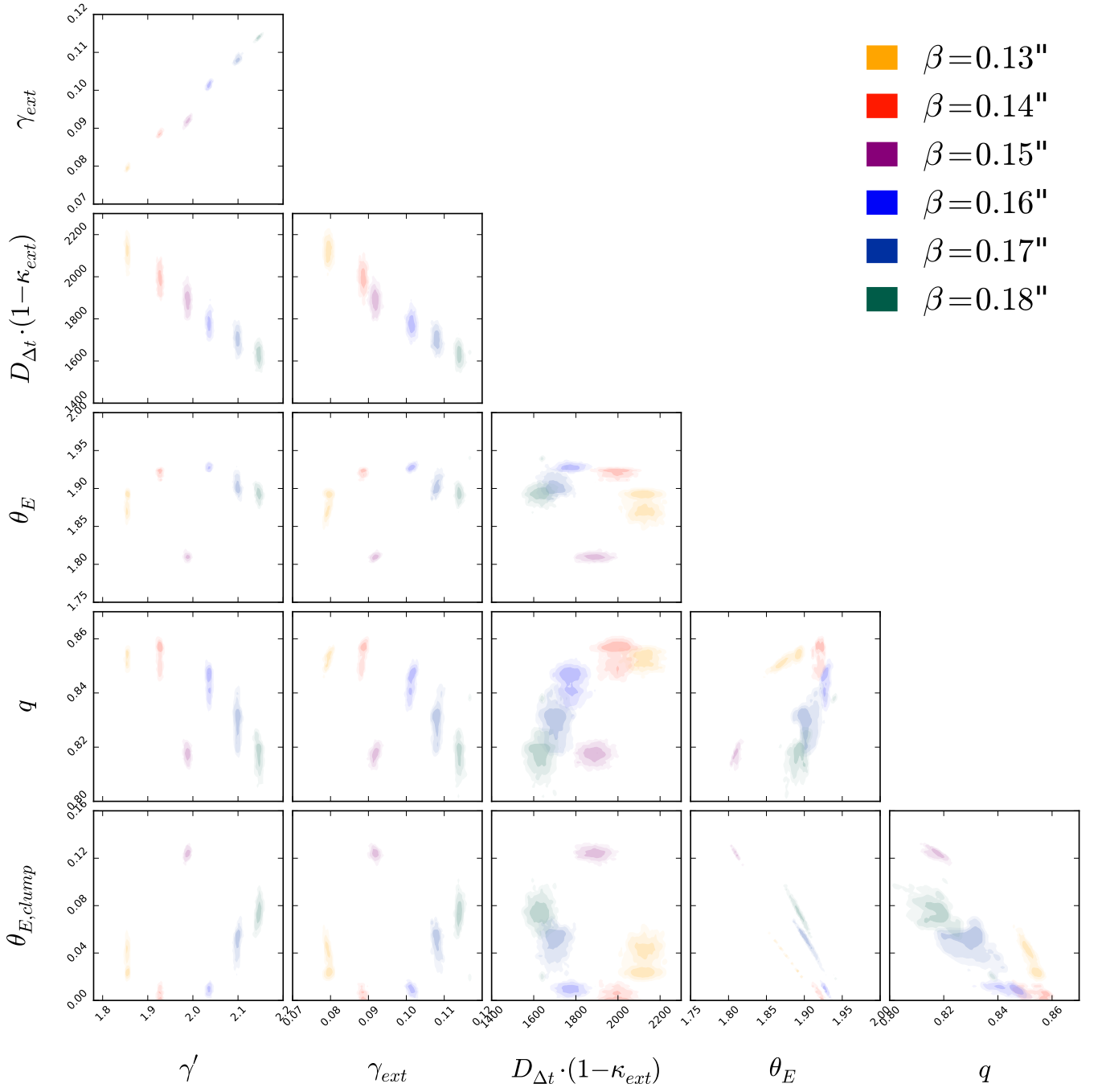


FIG. 12. Posterior distribution of lens model parameters and time delay distance of the combined analysis of imaging data of F555W and time delay measurements. Different colors correspond to different choices of the shapelet scale  $\beta$ . (same as Figure 5 for filter F814W).